Energy Storage Materials 76 (2025) 104161

Contents lists available at ScienceDirect

Energy Storage Materials

journal homepage: www.elsevier.com/locate/ensm

Homogeneous low-tortuosity membrane with fast ion transfer towards life-durable low-temperature zinc metal batteries

Yongzheng Zhang [a], Huiqing Zhou [a], Jianan Gu [b,*], Haifeng Yang [c], Xiaomin Cheng [c], Jing Zhang [d], Jitong Wang [a,*], Yanli Wang [a], Hongzhen Lin [c], Jian Wang [c,e,f,*], Liang Zhan [a,*], Licheng Ling [a]

[a] State Key Laboratory of Green Chemical Engineering and Industrial Catalysis, State Key Laboratory of Chemical Engineering, Key Laboratory of Specially Functional Polymeric Materials and Related Technology (Ministry of Education), Shanghai Key Laboratory of Multiphase Materials Chemical Engineering, East China University of Science and Technology, Shanghai 200237, China
[b] State Key Laboratory of Alternate Electrical Power System with Renewable Energy Sources, School of New Energy, North China Electric Power University, Beijing 100096, China
[c] i-Lab & CAS Key Laboratory of Nanophotonic Materials and Device, Suzhou Institute of Nano-Tech and Nano-Bionics, Chinese Academy of Sciences, Suzhou 215123, China
[d] School of Materials Science and Engineering, Xi'an University of Technology, Xi'an 710048, China
[e] Helmholtz Institute Ulm (HIU), Ulm D89081, Germany
[f] Karlsruhe Institute of Technology (KIT), Karlsruhe D76021, Germany

ARTICLE INFO

Keywords:
Zn metal battery
Boundary inhibition effect
Low tortuosity
Ion transfer pathways
Fast desolvation

ABSTRACT

Aqueous zinc metal batteries (AZMBs) have attracted significant attentions in the energy storage field due to their environmental safety. However, sluggish reaction kinetics of $Zn(H_2O)_6^{2+}$ desolvation and corresponding Zn^{2+} ion transfer hinder the low-temperature performance of AZMBs. Herein, the boundary inhibition effect of ion-related pathway is initially uncovered, and a homogeneous low-tortuosity separator membrane (LTSM) with enhanced kinetics of ion desolvation and transfer is proposed. This low-tortuosity structure of LTSM significantly enhances the effectiveness of pore sieving effect toward large $Zn(H_2O)_6^{2+}$ clusters, minimizing ion transfer barriers and homogenizing ion flux, as revealed by Raman and sum frequency generation spectroscopies. Encouragingly, the metallic Zn with LTSM exhibits lower nucleation overpotentials of ~50 mV, showcasing an ultralong lifespan of over 10,000 h at 0 °C. Even under −10 °C, a cycle life up to 5000 h is also achieved. The as-prepared full cells assembled with LTSM display the specific capacity of 200 mAh g^{-1} after 4000 cycles at 8 A g^{-1} under 0 °C. Increasing to 6.3 mg cm^{-2}, the large areal pouch cell stabilizes for 160 cycles with retained capacity of 315 mAh g^{-1}, demonstrating feasibility of eliminating the boundary inhibition effect with low-tortuosity separator membrane for practical applications.

1. Introduction

Zinc metal batteries (ZMBs) have gained significant attention in the energy storage field due to their abundant zinc resources, cost-effectiveness, and environmental safety [1–5]. The ability to operate in aqueous electrolytes with high electrochemical stability makes ZMBs particularly promising for large-scale energy storage systems [6–9]. However, the commonly used Zn anodes face some severe challenges such as the formation of Zn dendrites, unstable interfaces, and unwanted side reactions [10–13]. These issues are strictly related to the sluggish reaction kinetics of interfacial $Zn(H_2O)_6^{2+}$ desolvation and corresponding Zn^{2+} ion transfer and Zn atom plating (Fig. 1a), leading to low Coulombic efficiency and quick battery failure of ZMBs, posing obstacles to their practical application [14–17].

To deal with above issues, previous studies mainly focus on the challenges of Zn anodes, which are often surface-level symptoms rather than the underlying causes [18–23]. More experiments and theoretical analyses demonstrate that the Zn dendrites, the side reactions of hydrogen evolution reaction (HER) and interface corrosion should be attributed to the sluggish reaction kinetics of Zn^{2+} with corresponding

* Corresponding authors.
E-mail addresses: gujianan@ncepu.edu.cn (J. Gu), wangjt@ecust.edu.cn (J. Wang), wangjian2014@sinano.ac.cn, jian.wang@kit.edu (J. Wang), zhanliang@ecust.edu.cn (L. Zhan).

https://doi.org/10.1016/j.ensm.2025.104161
Received 2 January 2025; Received in revised form 17 February 2025; Accepted 5 March 2025
Available online 7 March 2025

higher barriers and the active water molecules in the solvation shell [24–27]. In spite of the construction strategies of catalysis and interphase , the stategy of pore sieving such as metal organic frameworks, hydrogen-bonded organic frameworks, and covalent organic frameworks are applied to enhance the dissociation kinetics [28–34]. However, ionic transport through these pore structures is random and constrained by the viscous force of the aqueous electrolytes, leading to the boundary layer inhibition effect. In this effect, the viscous forces in the electrolyte create a stagnant layer near the electrode surface, significantly impeding efficient ion transfer [35–37]. Specifically, the boundary layer thickness along the channel of these traditional protective coating layer is significantly enhanced owing to the strong viscous force, which is affected by twisted channels and uneven pore size distributions when $Zn(H_2O)_6^{2+}$ carriers cross the pathway in the layers (Fig. 1b(i)). Moreover, the boundary layers of diffusion are more prone to be overlapped within the random small channels, which further inhibits ion diffusion and significantly causes the problem of desolvation.

What's worse, as the temperature decreasing, the kinetic energy of solvent molecules increases dramatically, leading to a large solvation structure, where the solute ions are more tightly packed and the migration space is largely limited [38–40]. This change in the solvated structure amplifies the boundary layer inhibition effect, resulting in significant differences in solvent concentration and ion distribution between the boundary layer and the native electrolyte. Kinetically, the large solvated structure increases the activation energy for substance migration, making ion migration difficult and the diffusion rate decreases dramatically. In addition, this change indirectly interferes with the processes such as Zn^{2+} reduction and Zn^0 deposition on Zn anode, which is detrimental to the long-cycle stability and high-rate performance of ZMBs [41–44]. Therefore, it is of significance to design rational channels in the protective coating layer or separator to eliminate the serious boundary layer inhibition effect to modulate Zn^{2+} species kinetics, thus improving the low-temperature electrochemical performance of ZMBs.

Herein, a homogeneous low-tortuosity separator membrane (LTSM) with enhanced kinetics of ion desolvation and transfer is constructed on Zn anode to eliminate the boundary layer inhibition effect. The low-tortuosity structure significantly enhances the effectiveness of desolvation toward large $Zn(H_2O)_6^{2+}$ clusters, reducing the Zn^{2+} ion transfer barriers and homogenizes the ion flux against the boundary layer inhibition effect (Fig. 1b(ii)), as revealed by a series of *ex-situ/in-situ* spectral characterizations, optical observations and COMSOL simulations. Consequently, the symmetric Zn-LTSM anode with low-tortuosity ion transfer pathways exhibits an ultralong cycle life >10,000 h with a lower nucleation potential of ~50 mV at 0 °C. Even at −10 °C, the Zn-LTSM anode achieves a cycle life of up to 5000 h without any formation of Zn dendrite. Furthermore, the full cells assembled with Zn-LTSM anode stabilizes the capacity of 200 mAh g^{-1} for 4000 cycles at 8 A g^{-1} and impressive rate capability even at 0 °C. Impressively, a pouch cell with Zn-LTSM anode delivered a reversible specific capacity of 315 mAh g^{-1}, indicating the feasibility of eliminating the boundary layer inhibition effect with low-tortuosity separator membrane in low-temperature environments.

2. Results and discussion

As a representative selectively permeable membrane, the commercially available dialysis membrane was selected as the low-tortuosity separator membrane, which is primarily made from natural cellulose, a linear polysaccharide composed of numerous D-glucose units linked by 1,4-β-glycosidic bonds. As shown in Fig. 2a, each repeating unit in the cellulose molecular structure contains three free hydroxyl groups-one primary hydroxyl and two secondary hydroxyls, which contributes to its high hydrophilicity. Optical images of LTSM-8000 membrane exhibit a transparent feature **(Figure S1)**, where the value of "8000" refers to the molecular weight cut-off (MWCO), meaning the smallest molecular weight is able to effectively block, i.e., the largest molecular weight that is allowed to pass through the membrane. Therefore, the higher the MWCO, the larger the pore size will be. In virtue of scanning electron microscope (SEM), the LTSM-8000 coated on bare Zn exhibits a uniform and flat surface, while the bare Zn shows a coarse surface texture (**Figure S2**). The section-view of SEM image shows the thickness of LTSM-8000 is ~85 μm (**Figure S3**), which is far thinner than commercial glass fiber separator (~680 μm). Additionally, Fourier transform infrared (FTIR) spectrum of LTSMs immersed in 2 M $ZnSO_4$ electrolyte reveals a blue shift in the H—O stretching vibration compared to that of the pure electrolyte (Fig. 2b), signifying enhanced hydrogen bond formation between LTSM and water solvent in the electrolyte. The increased hydrogen bonding interaction of O—H between LTSMs and water disrupts the original water-water hydrogen network, significantly

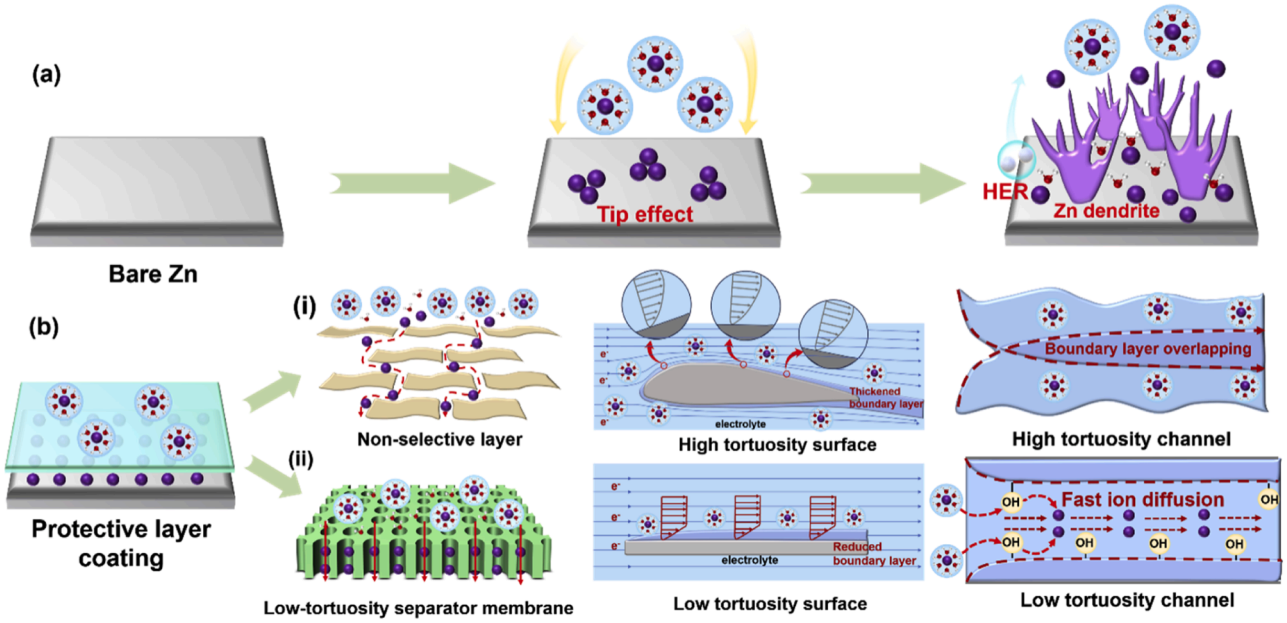

Fig. 1. (a) The Zn deposition behavior on bare Zn anode. (b) Protective layer coating on Zn anode by (i) non selective layer; (ii) low tortuosity separator membrane.

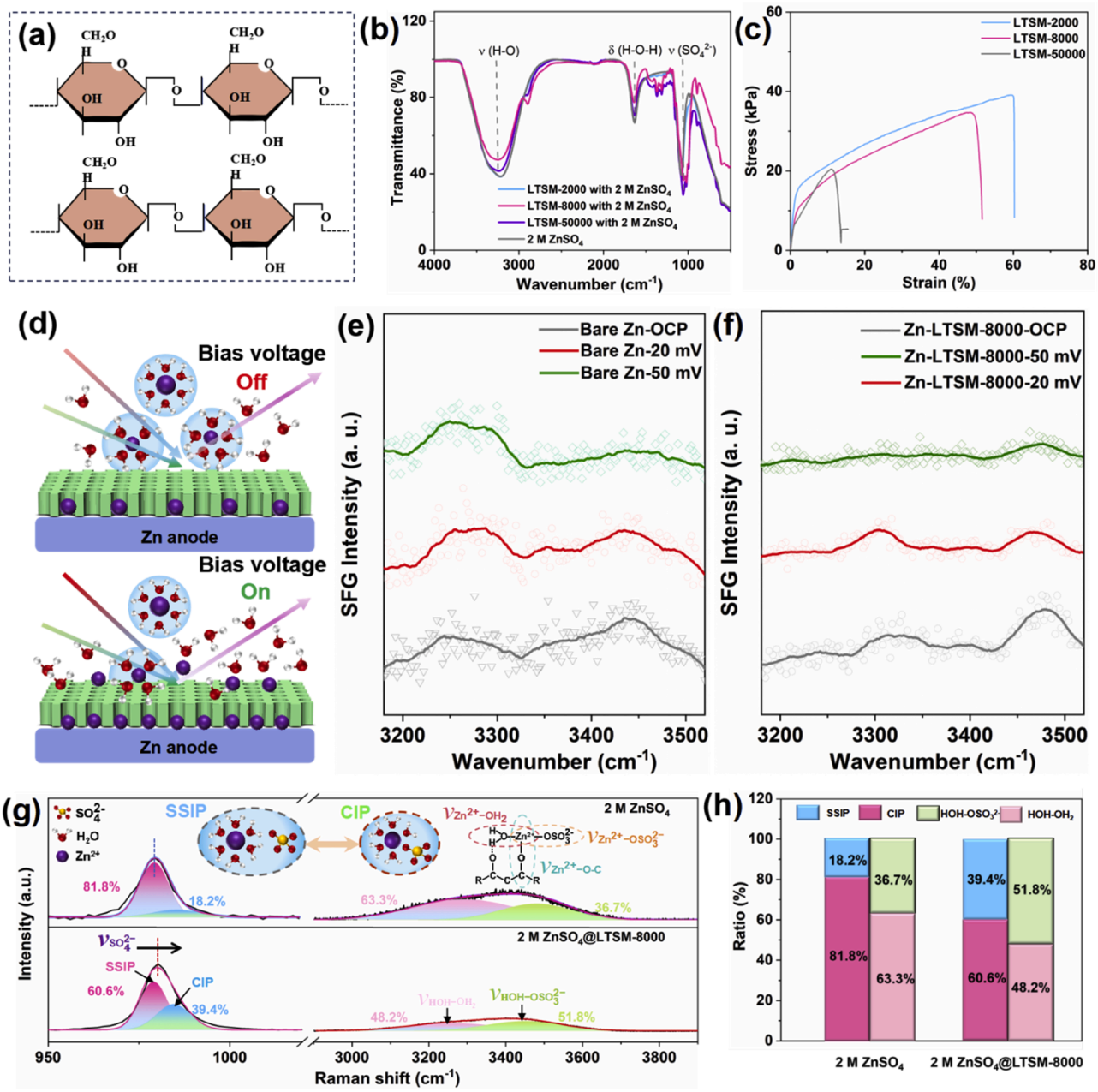

Fig. 2. (a) Schematic illustration the molecular structure of the low-tortuosity membrane. (b) FTIR spectra of low-tortuosity membrane within aqueous electrolyte. (c) Stress-strain curves for low-tortuosity membrane with varying molecular weight cut-off. (d) Schematic illustration of the *in-situ* SFG on the Zn-LTSM-8000/electrolyte interface with/without bias voltage. The SFG spectra of the O—H bond signal on (e) bare Zn/electrolyte and (f) Zn-LTSM-8000/electrolyte interface with/without bias voltage. (g) Raman spectra on the 2 M $ZnSO_4$ and 2 M $ZnSO_4$@LTSM-8000. (h) The ratio summary of SSIP, CIP, O—H stretch vibrations in different systems.

reducing the activity of active H_2O to mitigate side reactions [45]. Furthermore, the red shift of the SO_4^{2-} peak suggests an increase in free SO_4^{2-} ions (Fig. 2b), due to the enhanced separation of Zn^{2+}-SO_4^{2-} ion pairs. As exhibited in Fig. 2c, stress-strain curves reveal that the mechanical strength of low-tortuosity membrane decreases as the molecular weight cut-off increases. Benefiting from the moderate pore structure, LTSM-8000 can endure a strain of 48 % under a stress of 34.5 kPa, which is enough to bear the stress generated by the repeated Zn plating and stripping [46].

The interfacial desolvation process is observed through a range of spectroscopic analysis. As a typical interface-sensitive technology, *in-situ* sum frequency generation (SFG) spectroscopy is performed on different electrolyte/anode interfaces to dynamically investigate the evolutions in water molecules [47–49]. Fig. 2d illustrates the status variations of $[Zn(H_2O)_6]^{2+}$ at the electrode/electrolyte interface driven by bias voltage, detecting the state of the interfacial water molecules. Obvious solvent peaks arising from the stretching vibrations of the O—H bonds are observed in the range of 3200–3500 cm^{-1} [50]. Once applying the bias voltages on the systems, the peak located at 3320 cm^{-1} exhibits a significant intensity decrease at the electrolyte/Zn-LTSM-8000 interface, signifying the weakened association of Zn^{2+} with the strongly bound solvated water by LTSM-8000, so does the weakly bound solvated water molecules within the solvation shell centered around 3450 cm^{-1} (Figs. 2f). At the same time, higher bias voltage allows better desolvation and sieving capability, while negligible changes of the peak's intensity is captured at the bare Zn/electrolyte interface with the bias voltage on or

off (Figs. 2e). This interfacial behavior indicates that the presence of the LTSM on Zn anode greatly facilitates the disassociation of Zn^{2+} ions from the solvation sheath, resulting in accelerated interfacial kinetics. In addition, Raman spectroscopy (Fig. 2g) also reveals an obvious increase from solvent separated ion pairs (SSIP) to contact ion pairs (CIP) at the Zn-LTSM-8000/electrolyte interface, suggesting a closer contact of [$Zn^{2+}SO_4^{2-}$] ion pairs induced by LTSM. Besides, the O—H stretching vibration in the range of 3000–3800 cm^{-1} exhibits an increasing ratio of HOH—OSO_3^{2-} stretch peaks from 36.7 % to 51.8 % by introducing the LTSM (Fig. 2h) [51]. Through enhancing the interaction of LTSM with H_2O molecules and SO_4^{2-}, strong hydrogen bonding interactions are developed to inhibit the water activity and hinders the participation of SO_4^{2-} in the solvation structure of Zn^{2+}, thus inhibiting the hydrogen evolution reaction of active water and suppressing the other by-products reactions to improve the stability of the interface [51]. Moreover, benefiting from the enhanced interfacial desolvation behavior by LTSM, the Zn^{2+} transference number was improved from 0.39 to 0.62 (Figure S4), implying better ion transport efficiency and fast kinetics.

The accelerated interfacial desolvation behavior is helpful to achieve good electrochemical performance of Zn-LTSM anodes. As shown in Fig. 3a, due to the abundant hydroxyl groups in LTSM-8000, the Zn-LTSM-8000 exhibits good affinity with the aqueous electrolyte to provide a much lower contact angle of 24.5° than that of bare Zn (90.0°). Such good hydrophilicity may contribute a lot to trap active water, thus facilitating abundant free Zn^{2+} to pass through ion channels within LTSM to benefit further Zn nucleation and growth during the deposition

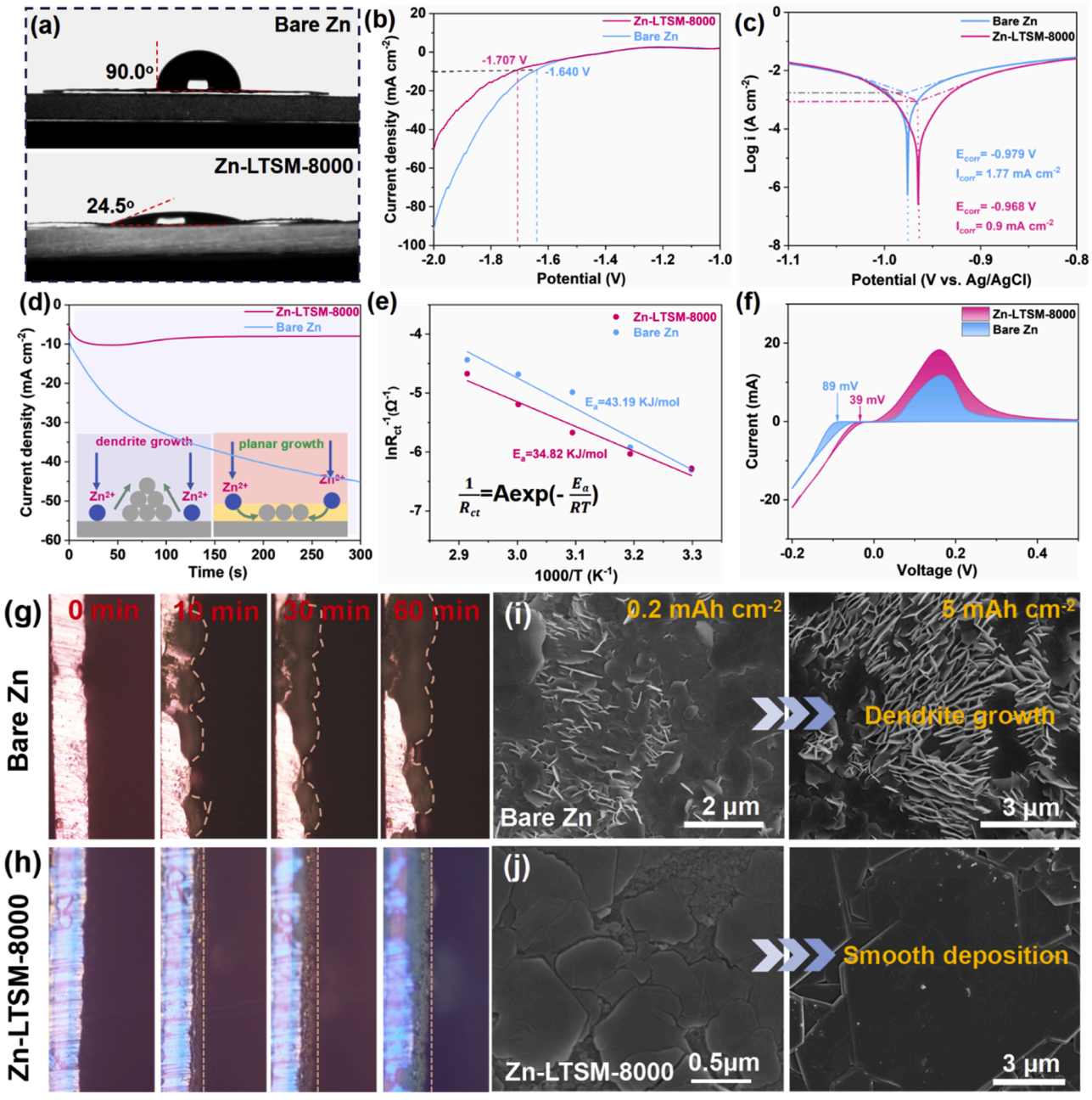

Fig. 3. (a) Contact angles of aqueous electrolyte on Zn-LTSM-8000 and bare Zn anodes. (b) Linear sweep voltammetry curves of Zn-LTSM-8000 and bare Zn anodes. (c) Tafel curves of Zn-LTSM-8000 and bare Zn anodes, respectively. (d) CA curves of Zn-LTSM-8000 and bare Zn anodes under −0.15 V. (e) Activation energy of symmetric cells using Zn-LTSM-8000 and bare Zn anodes, respectively. (f) CV curves of Zn-LTSM-8000//Cu and bare Zn//Cu cells. *In-situ* optical observations of (g) bare Zn and (h) Zn-LTSM-8000 anodes with different Zn plating capacities. *Ex-situ* SEM images of Zn plating on (i) bare Zn anodes and (j) Zn-LTSM-8000 anodes at various capacities, respectively.

process. As shown in Fig. 3b, the Zn-LTSM-8000 electrode shows a more negative onset potential than bare Zn electrode (−1.707 vs. −1.640 V) at 10 mA cm^{-2}, indicating the low-tortuosity membrane can efficiently suppress the HER to release any H_2, agreeing well with the spectral analysis results. Tafel curves (Fig. 3c) suggest that the Zn-LTSM-8000 anode has a better corrosion resistance to the electrolyte due to both the lower corrosion voltage and lower corrosion current density (−0.968 V/0.90 mA cm^{-2} vs. −0.979 V/1.77 mA cm^{-2}). SEM images of the Zn-LTSM-8000 and bare Zn electrodes after immersion in aqueous electrolyte for one week further validate this observation (**Figure S5)**. The Zn-LTSM-8000 electrode maintains a relatively uniform surface in contrast to the significant corroded bare Zn surface, suggesting that the LTSM can highly stabilize the aqueous electrolyte without unexpected corrosions. Such good corrosion resistance of the Zn-LTSM-8000 anode better sweeps the obstacles for better Zn nucleation and following deposition processes. As a result, subsequent Zn deposition occurs in a preferential planar growth mode rather than a random growth pattern, as described in the growth model inset (Fig. 3d). The expected planar growth of Zn on Zn-LTSM-8000 electrode should be attributed to the reduced activation energy (34.82 vs. 43.19 kJ mol^{-1}) for the Zn^{2+} desolvation and diffusion during Zn stripping/plating processes (**Figures 3e** and **S6, Table S1**). Meanwhile, the cyclic voltammetry (CV) curve of Zn-LTSM-8000//Cu half-cell shows a lower polarization of 39 mV (Fig. 3f), whilst a higher peak current indicates more nucleation sites and faster diffusion on the Zn-LTSM-8000 anode surface. Furthermore, the planar growth mode is confirmed by *in-situ* optical and *ex-situ* SEM images of Zn deposition at different capacities on Zn-LTSM-8000 anode. As displayed in Fig. 3g, over a plating time from 0 to 60 min, the bare Zn anode exhibits an uneven surface characterized by numerous Zn dendrites, while the surface of the Zn-LTSM-8000 anode maintains a flat morphology with only a uniform increase in the thickness of the deposited Zn layer (Fig. 3h). The SEM images of Zn plating at different capacities from 0.2 to 5 mAh cm^{-2} on the Zn-LTSM-8000 anodes also exhibits uniform planar growth against random growth on pristine Zn surfaces (Figs. 3i and 3j). Besides, the low-resolution SEM image of Zn-LTSM-8000 anode after plating 5 mAh cm^{-2} exhibits more

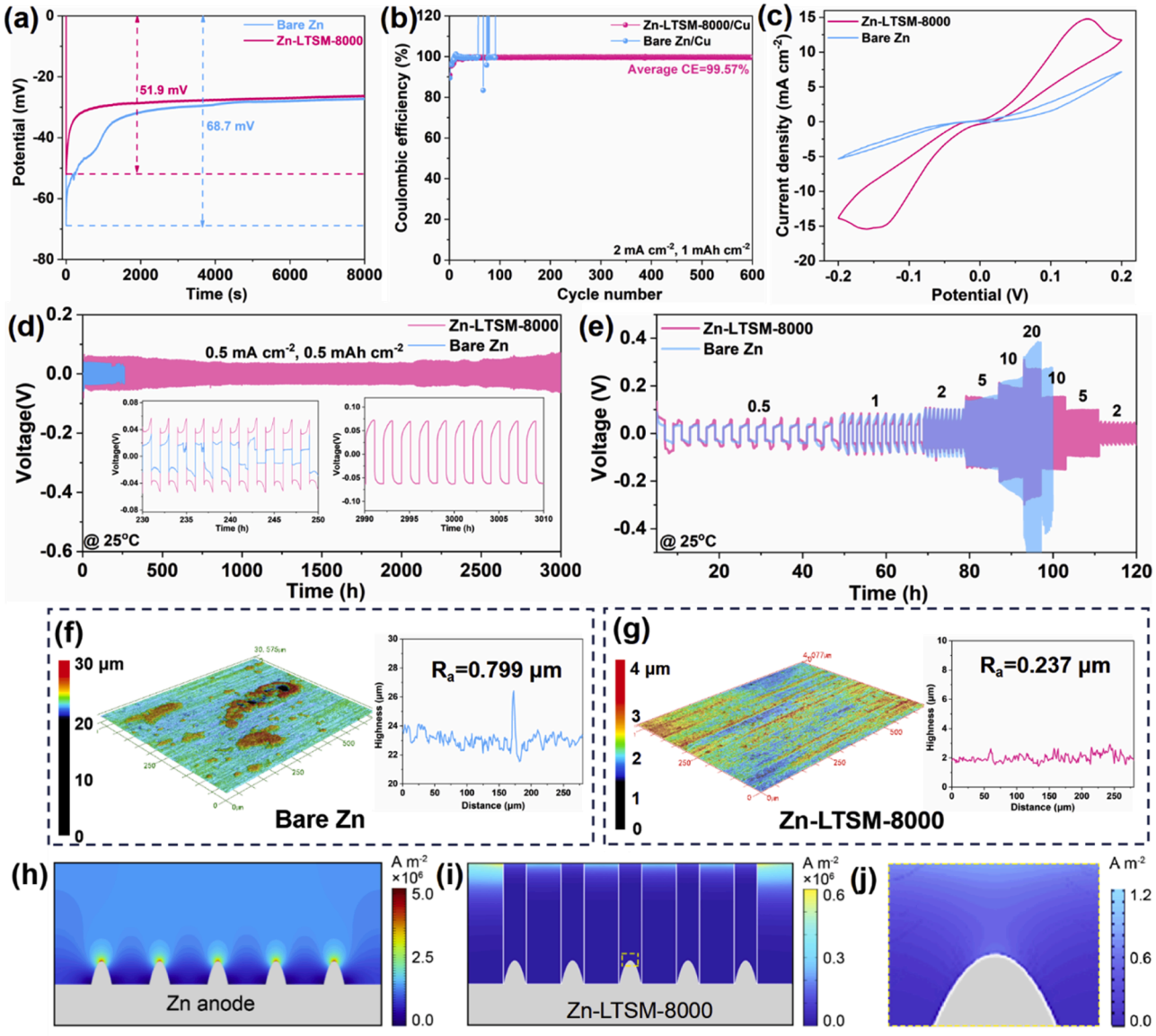

Fig. 4. (a) Nucleation overpotentials of Zn-LTSM-8000 and bare Zn anodes at 1 mA cm^{-2}. (b) CE of Zn-LTSM-8000//Cu and bare Zn//Cu, respectively. (c) CV curves of symmetric cells of Zn-LTSM-8000 and bare Zn anodes. (d) Cycling performance and (e) rate capability of Zn-LTSM-8000 symmetric cells. 3D maps of (f) Zn-LTSM-8000 and (g) bare Zn anodes after Zn deposition. COMSOL Multiphysics simulation of Zn deposition on (h) bare Zn anode and (i) Zn-LTSM-8000 anode. (j) Magnified COMSOL Multiphysics simulation in (i).

homogeneous Zn deposition than that of bare Zn anode (**Figure S7**).

Chronoamperometry measurements were then performed to compare the nucleation and growth behaviors of Zn on Zn-LTSM-8000 and bare Zn anodes. As shown in Fig. 4a, the Zn-LTSM-8000 anode displays a lower nucleation overpotential of 51.9 mV than bare Zn anode (68.7 mV), indicating smaller nucleation barrier needed for Zn nucleation on Zn-LTSM-8000 anode so as to promote uniform Zn nucleation at the initial deposition process. Subsequently, Coulombic efficiency (CE) measurement of Zn-LTSM-8000//Cu and bare Zn//Cu asymmetric cells were conducted. The Zn-LTSM-8000//Cu exhibits an average CE of ~ 99.6 % during the 600 cycles (**Figures 4b** and **S8**). However, bare Zn//Cu asymmetric cell quickly fails <100 cycles. The CV curves of Zn-LTSM-8000 symmetric cells further demonstrate enhanced reaction activity for the Zn^{2+}/Zn^{0} redox process on Zn-LTSM-8000 anode in comparison to bare Zn anode (Fig. 4c), which indicates that the introduction of the low-tortuosity membrane promotes the diffusion kinetics for superior electrochemical performance.

To investigate the electrochemical performance of Zn-LTSM anodes, symmetric cells with varying molecular weight cut-off were evaluated. As shown in **Figure S9a**, all the three Zn-LTSM anodes display excellent cycling stability of >1500 h at a current density of 0.2 mA cm^{-2}. Among them, the Zn-LTSM-8000 anode exhibits the longest cycle life of 2000 h with lowest overpotential of 38 mV. The superior cycling performance of Zn-LTSM-8000 is attributed to its moderate pore size structure to trade-off ionic conductivity and desolvation efficiency, providing the largest ionic conductivity (**Figure S9b** and **S9c**). Besides, the pore structure was further confirmed by the small-angle X-ray diffraction measurements. As shown in **Figure S10**, both LTSM-50000 and LTSM-8000 exhibit distinct diffraction peaks at 2θ <1.0°, indicating their highly ordered porous structures. The broader and more intense peak of LTSM-8000 suggests a higher degree of structural order and porosity. Since peak width is inversely correlated with grain size, this implies that LTSM-8000 has smaller grains and possibly smaller pore diameters, agreeing well with the definition of MWCO. Furthermore, increasing the current density to 0.5 mA cm^{-2} (Fig. 4d) or 1 mA cm^{-2} (Figure S11), the Zn-LTSM-8000 anode also demonstrates good cycling stability, >3000 h and 1200 h, respectively, illustrating the excellent performance of Zn-LTSM-8000 under varying operational conditions. Besides, we also conducted the performance of Zn symmetric cells with LTSM-8000 possessing thicknesses of 170 μm and 40 μm under 0.5 mA cm^{-2} and 0.5 mAh cm^{-2} (**Figure S12**). The results indicate that the previously used 85 μm membrane in our study exhibits the best performance (Fig. 4d). Galvanostatic intermittent titration technique (GITT) profiles in **Figurer S13** shows an initial voltage rise that stabilizes within 3 min. The Zn-LTSM-8000 anode shows a lower total polarization of 50.5 mV and reduced concentration polarization of 8.2 mV, suggesting better interfacial stability and more efficient ion diffusion. These results highlight that Zn-LTSM-8000 anode offers superior electrochemical performance by reducing polarization and improving Zn^{2+} transport. More importantly, the Zn-LTSM-8000 anode can withstand a high current density of 20 mA cm^{-2} with an overpotential of ~270 mV (**Figure 4e** and **S14**). By contrast, the bare Zn anode experiences significant voltage fluctuations and finally short circuit at 20 mA cm^{-2}.

To enclose the electrochemical mechanism of LTSM on Zn anode, the 3D surface maps of both the Zn-LTSM-8000 and bare Zn anodes after repeated Zn plating/stripping are given in Figs. 4f and 4g. The surface of Zn-LTSM-8000 anode exhibits much smaller roughness compared to bare Zn anode, implying good consistent with the planar growth model as well as the *ex-situ* SEM observations. The low-tortuosity membrane not only provides fast ion pathways for Zn^{2+} but also helps hinder side reactions in aqueous ZMBs, as further simulated by COMSOL Multiphysics simulations of Zn plating on both Zn-LTSM-8000 and bare Zn anodes (Figs. 4h–4j). The bare Zn anode exhibits a significant electric field and a steep gradient in Zn^{2+} flux across its surface (Fig. 4h). In contrast, after coating a uniform low-tortuosity membrane (Figs. 4i and 4j), the Zn-LTSM-8000 anode displays a homogeneous electric field and a more uniform gradient of Zn^{2+} flux. Besides, XRD measurements were performed on Zn-LTSM-8000 anode and bare Zn anode after cycling (**Figure S15a**). XRD patterns reveal that the cycled Zn-LTSM-8000 anode exhibits distinct Zn diffraction peaks, indicating a well-maintained crystalline structure. In contrast, the cycled bare Zn presents additional peaks corresponding to $Zn_4S_2O_4(OH)_6{\cdot}4H_2O$, suggesting the formation of byproducts that may lead to performance degradation. Furthermore, Time-of-flight secondary ion mass spectrometry (TOF-SlMS) analysis further demonstrates the differences in surface composition. The bare Zn (**Figure S15b**) exhibits a non-uniform ZnO^{-} distribution, while the Zn-LTSM-8000 anode shows a more homogeneous ZnO^{-} signal (**Figure S15c**), suggesting improved surface stability and mitigated side reactions.

The Zn-LTSM-8000 anode were further tested at low temperatures to verify its temperature robustness. As shown in Fig. 5a, Zn-LTSM-8000 anode demonstrates excellent cycle life of over 10,000 h at 0.5 mA cm^{-2} under the temperature of 0 °C. Besides, when the temperature is increased to 25 °C, the overpotential decreases from 100 mV to 70 mV, and returning to 0 °C drives the overpotential to recover. This phenomenon is also the same under 1 mA cm^{-2} and 1 mAh cm^{-2} (**Figure S16**), indicating that the low-tortuosity membrane quickly adapts to changes in external temperature to maintain the stable interfacial desolvation and Zn^{2+} diffusion for reversible low temperature reactions. Even when the current density and capacity are increased to 5 mA cm^{-2} and 5 mAh cm^{-2}, the Zn-LTSM-8000 anodes still exhibit a long cycle life up to 1000 h (**Figure S17**). The low-tortuosity membrane endowed the Zn anode with superior electrochemical performance than most of the reported works (Fig. 5b). Besides, the Zn-LTSM-8000 symmetric cell maintains a lower overpotential of ~260 mV at low temperature even at 10 mA cm^{-2} (Fig. 5c), while the bare Zn symmetric cell experiences large voltage fluctuation and finally fails to work, confirming the excellent low-temperature robustness of the Zn-LTSM-8000 anode. Lowering the operation temperature to −10 °C (Fig. 5d), Zn-LTSM-8000 anodes with $Zn(OTF)_2$ electrolyte achieved an ultralong cycle life of up to 5000 h. Returning the temperature to 25 °C, the symmetric cell of Zn-LTSM-8000 still works well. The reduced charge transfer resistance of Zn-LTSM-8000 symmetrical cell at low temperature further suggests improved interfacial stability and facilitated ion transport, contributing to superior electrochemical performance under practical conditions (**Figure S18** and **Table S2**).

In paring with δ-$K_{0.51}V_2O_5$ (KVO) cathodes, the Zn-LTSM-8000//KVO full cell in Fig. 5e delivers an impressive rate performance at 0 °C with a reversible capacity of ~172 mAh g^{-1} even at a high current density of 8 A g^{-1} (**Figure S19**). Moreover, Zn-LTSM-8000//KVO full cell demonstrates an ultra stable low-temperature capacity of 200 mAh g^{-1} after 4000 cycles at 8 A g^{-1} with nearly a 100 % CE (**Figures 5f** and **S20**). To gain deeper insights, SEM measurements were conducted on cycled anodes and cathodes of Zn-LTSM-8000//KVO and bare Zn//KVO cells. Typically, the surfaces of both the anode and cathode in Zn-LTSM-8000//KVO cells exhibit a smooth and uniform morphology (**Figure S21**), while those in the bare Zn//KVO cells show a coarse and uneven texture (**Figure S22**). The CV profiles at different scanning rates for full cells with bare Zn or Zn-LTSM-8000 reveal their electrochemical behavior and charge storage mechanisms (**Figure S23**). For the Zn-LTSM-8000//KVO cell, diffusion dominates at all scan rates, contributing up to 78.7 % at 0.1 mV s^{-1}. In contrast, bare Zn//KVO cell shows higher capacitance contribution, especially at lower scan rates, limiting its performance at higher rates due to slower ion diffusion. Zn-LTSM-8000//KVO cell exhibits superior electrochemical performance, particularly at high scan rates, due to efficient ion diffusion, while bare Zn//KVO cell is hindered by surface capacitance.

Further lowering the environmental temperature to 0 °C, the Zn-LTSM-8000//KVO full cell with high loading cathode (6.6 mg cm^{-2}) performs for >250 cycles with a stable capacity of 255 mAh g^{-1} at 1 A g^{-1} (**Figures 5g** and **S24**). Even at −10 °C, it still maintains functionality for 200 cycles, except for a reduction in specific capacity (**Figure S25**).

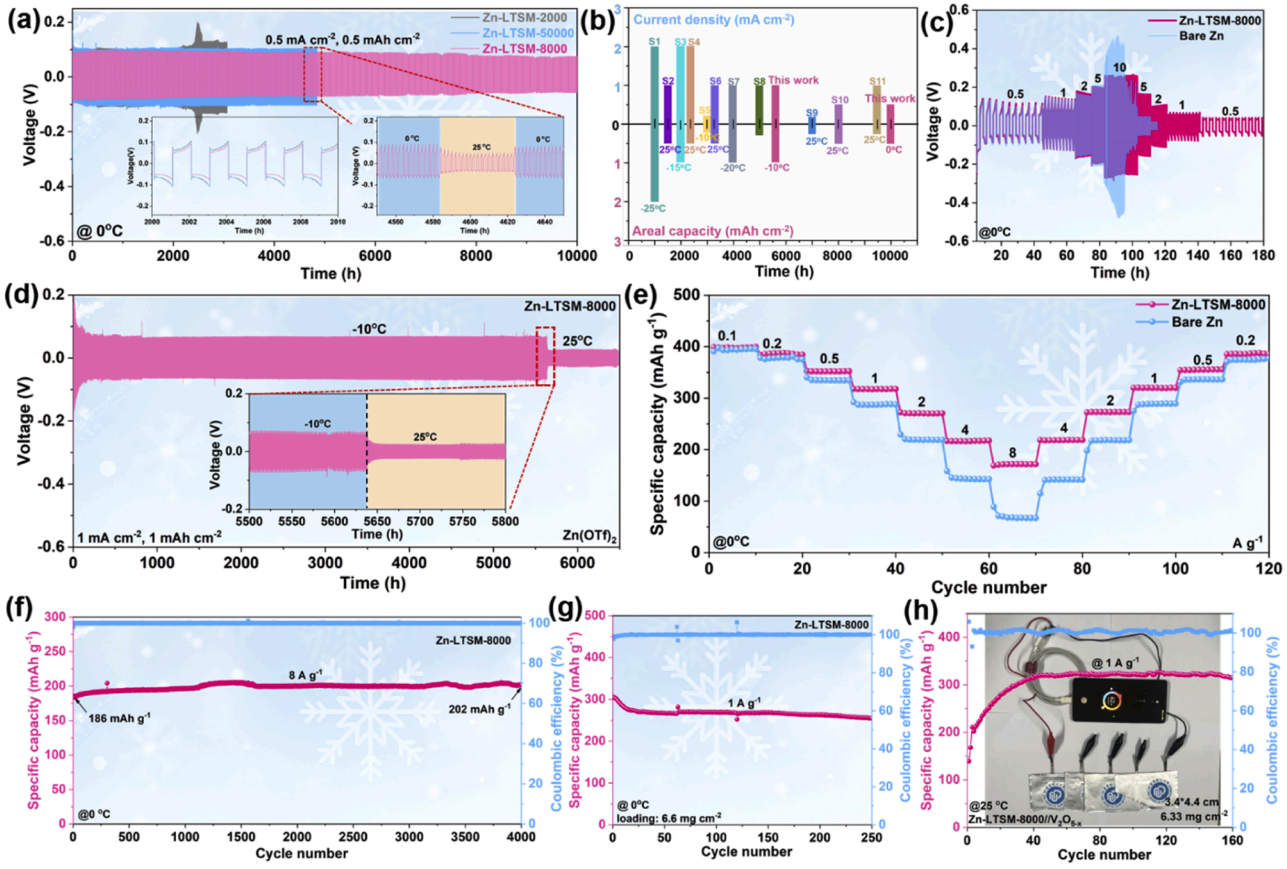

Fig. 5. (a) Cyclic performance of Zn-LTSM symmetrical cells at 0.5 mA cm^{-2} and 0.5 mAh cm^{-2} under the temperature of 0 °C. (b) Electrochemical performance comparison between Zn-LTSM-8000 and reported Zn anodes. (c) Rate performance of Zn-LTSM-8000 symmetrical cells at the temperature of 0 °C. (d) Cyclic performance of Zn-LTSM-8000 cell with $Zn(CF_3SO_3)_2$ electrolyte at 1.0 mA cm^{-2} under the temperature of −10 °C. (e) Rate and (f) long-term cyclic performance of full cells composed of Zn-LTSM-8000 anode and KVO cathode at 0 °C. (g) Cyclic performance of full cell composed of Zn-LTSM-8000 anode and high-loading KVO cathode with 6.6 mg cm^{-2} at 0 °C. (h) Cyclic performance of pouch cell composed of Zn-LTSM-8000 anode and commercial V_2O_{5-x} cathode at a current density of 1 A g^{-1}, inset: image of the as-fabricated pouch cell powering a smart device.

These above results demonstrate that the Zn-LTSM-8000 anode can operate effectively under low-temperature conditions, highlighting its application potential in extreme environments. To pursuit its practical applications, pouch cells were assembled in Fig. 5h. The Zn-LTSM-8000 modulated pouch cells are able to power a smart phone. Additionally, the Zn-LTSM-8000//KVO pouch cell with mass loading of 6.33 mg cm^{-2} demonstrates a high reversible specific capacity of 316 mAh g^{-1} by the 160th cycle.

To further explore the possibility of LTSM as an alternative to replace glassfiber separator, as shown in **Figure S26a**, the cycling stability was still maintained (>500 h) and better than bare Zn with glassfiber separator (fails to work at about 250 h, Fig. 4d). For the full cells assembled with KVO cathode and Zn-LTSM-8000, little capacity difference can be observed with or without glassfiber separator (**Figure S26b**). Besides, the Zn-LTSM-8000//KVO cell without glassfiber separator also exhibits stable cycle performance at 10 A g^{-1} for >800 cycles (**Figure S26c**), demonstrating the feasibility of using this membrane as a replacement for commercial separators.

3. Conclusion

In conclusion, the homogeneous ion transfer pathways on Zn anodes using a low-tortuosity separator membrane to eliminate the boundary inhibition effect is initially proposed. This low-tortuosity structure significantly reduces the desolvation energy barrier of $Zn(H_2O)_6^{2+}$ clusters across the boundary layer, minimizes the ion transfer barrier and guides the lateral deposition of zinc ions, as confirmed by various COMSOL simulations, electrochemical evaluation, *ex-situ* Raman spectroscopy as well as *in-situ* sum frequency generation and optical observations. As a result, symmetric Zn anode with low-tortuosity ion transfer pathways exhibits a lower overpotential of 50 mV for an ultralong cycle life >10,000 h at 0 °C. Even at −10 °C, the Zn-LTSM anode achieves a cycle life of up to 5000 h. Furthermore, at a low temperature of 0 °C, the Zn-LTSM-8000//KVO full cells deliverer a rate capability of 172 mAh g^{-1} at 8 A g^{-1} and stable capacity of 200 mAh g^{-1} for 4000 cycles at 8 A g^{-1} without capacity attenuation. At an increasing mass loading of 6.6 mg cm^{-2}, the KVO cathode with Zn-LTSM-8000 anode still maintains 255 mAh g^{-1} after 250 cycles at 1 A g^{-1}. Impressively, the as-fabricated pouch cell with Zn-LTSM-8000 anode stabilizes for 160 cycles with a reversible specific capacity of 315 mAh g^{-1}, indicating potential of eliminating the boundary inhibition effect with low-tortuosity separator membrane for accelerating desolvation kinetics in practical applications.

CRediT authorship contribution statement

Yongzheng Zhang: Writing – original draft, Investigation, Funding acquisition, Data curation. **Huiqing Zhou:** Writing – original draft, Investigation, Data curation. **Jianan Gu:** Writing – review & editing, Investigation, Funding acquisition, Data curation. **Haifeng Yang:** Investigation, Data curation. **Xiaomin Cheng:** Investigation, Funding acquisition, Data curation. **Jing Zhang:** Writing – review & editing, Funding acquisition. **Jitong Wang:** Writing – review & editing, Supervision, Funding acquisition. **Yanli Wang:** Writing – review & editing,

Supervision, Funding acquisition. **Hongzhen Lin:** Methodology, Funding acquisition. **Jian Wang:** Writing – review & editing, Investigation, Funding acquisition, Data curation. **Liang Zhan:** Methodology, Funding acquisition, Data curation. **Licheng Ling:** Supervision, Methodology.

Declaration of competing interest

The authors declare that they have no known competing financial interests or personal relationships that could have appeared to influence the work reported in this paper.

Acknowledgments

This work was financially supported by the National Key R&D Program of China (2021YFA1201503), National Natural Science Foundation of China (22075081, 52372045, 52102203, 22178116, 62474064, 22279161), China Postdoctoral Science Foundation (No. 2023M731084, 2024M762318), Shanghai Sailing Program of China (23YF1408900), the Natural Science Foundation of Jiangsu Province (BK. 20210130), Shanghai Sailing Program of China (23YF1408900), the Key R&D Program of Jiangsu Province (BG2024020) and the Opening funding from Key Laboratory of Engineering Dielectrics and Its Application (Harbin University of Science and Technology) (No. KFM202507, Ministry of Education). Dr. J. Wang also acknowledge the funding provided by the Alexander von Humboldt Foundation. Y. Z. thanks the Shanghai Super Postdoctoral Incentive Program. The authors thank the Research Center of Analysis and Test of East China University of Science and Technology for the assistance with the characterization. We also thank the technical support from Nano-X, Suzhou Institute of Nano-tech and Nano-bionics, Chinese Academy of Sciences.

Supplementary materials

Supplementary material associated with this article can be found, in the online version, at doi:10.1016/j.ensm.2025.104161.

Data availability

Data will be made available on request.

References

[1] J. Gu, Y. Shi, Z. Du, M. Li, S. Yang, Stress relief in metal anodes: mechanisms and applications, Adv. Energy Mater 13 (2023) 2302091.
[2] H. Li, S. Li, R. Hou, Y. Rao, S. Guo, Z. Chang, H. Zhou, Recent advances in zinc-ion dehydration strategies for optimized Zn–metal batteries, Chem. Soc. Rev. 53 (2024) 7742–7783.
[3] Z. Zheng, X. Zhong, Q. Zhang, M. Zhang, L. Dai, X. Xiao, J. Xu, M. Jiao, B. Wang, H. Li, Y. Jia, R. Mao, G. Zhou, An extended substrate screening strategy enabling a low lattice mismatch for highly reversible zinc anodes, Nat. Commun. 15 (2024) 753.
[4] Y. Dai, R. Lu, C. Zhang, J. Li, Y. Yuan, Y. Mao, C. Ye, Z. Cai, J. Zhu, J. Li, R. Yu, L. Cui, S. Zhao, Q. An, G. He, G.I.N. Waterhouse, P.R. Shearing, Y. Ren, J. Lu, K. Amine, Z. Wang, L. Mai, Zn^{2+}-mediated catalysis for fast-charging aqueous Zn-ion batteries, Nat. Catal. 7 (2024) 776–784.
[5] H. Wang, Y. Chen, H. Yu, W. Liu, G. Kuang, L. Mei, Z. Wu, W. Wei, X. Ji, B. Qu, L. Chen, A multifunctional artificial interphase with fluorine-doped amorphous carbon layer for ultra-stable Zn anode, Adv. Funct. Mater. 32 (2022) 2205600.
[6] L. Jia, H. Hu, X. Cheng, H. Dong, H. Li, Y. Zhang, H. Zhang, X. Zhao, C. Li, J. Zhang, H. Lin, J. Wang, Toward low-temperature zinc-ion batteries: strategy, progress, and prospect in vanadium-based cathodes, Adv. Energy Mater. 14 (2023) 2304010.
[7] J. Gu, Y. Zhang, Y. Shi, Y. Jin, H. Chen, X. Sun, Y. Wang, L. Zhan, Z. Du, S. Yang, M. Li, Heteroatom immobilization engineering toward high-performance metal anodes, ACS Nano 18 (2024) 25966–25985.
[8] H. Dai, T. Sun, J. Zhou, J. Wang, Z. Chen, G. Zhang, S. Sun, Unraveling chemical origins of dendrite formation in zinc-ion batteries via in situ/operando X-ray spectroscopy and imaging, Nat. Commun. 15 (2024) 8577.
[9] Y. Guo, C. Luo, M. Yang, H. Wang, W. Ma, K. Hu, L. Li, F. Wu, R. Chen, Dynamic covalent bonds regulate zinc plating/stripping behaviors for high-performance zinc ion batteries, Angew. Chem. Int. Ed. 63 (2024) e202406597.
[10] W. Yang, Y. Yang, H. Yang, H. Zhou, Regulating water activity for rechargeable zinc-ion batteries: progress and perspective, ACS Energy Lett. 7 (2022) 2515–2530.
[11] J. Gu, Y. Tao, H. Chen, Z. Cao, Y. Zhang, Z. Du, Y. Cui, S. Yang, Stress-release functional liquid metal-MXene layers toward dendrite-free zinc metal anodes, Adv. Energy Mater. 12 (2022) 2200115.
[12] H. Yan, S. Li, Y. Nan, S. Yang, B. Li, Ultrafast zinc-ion-conductor interface toward high-rate and stable zinc metal batteries, Adv. Energy Mater. 11 (2021) 2100186.
[13] Z. Wu, Y. Zuo, Y. Zhang, X. Li, J. Zhang, Y. Wang, C. Shen, X. Cheng, M. Liu, H. Liu, H. Lin, J. Wang, L. Zhan, L. Ling, Modulating inner Helmholtz layer by electrocatalytically sieving $[Zn(H_2O)_6]^{2+}$ for 10000-cycle zinc-ion hybrid capacitors under extremely harsh conditions, Energy Storage Mater 70 (2024) 103463.
[14] L. Wang, B. Zhang, W. Zhou, Z. Zhao, X. Liu, R. Zhao, Z. Sun, H. Li, X. Wang, T. Zhang, H. Jin, W. Li, A. Elzatahry, Y. Hassan, H. Fan, D. Zhao, D. Chao, Tandem chemistry with Janus Mesopores Accelerator for efficient aqueous batteries, J. Am. Chem. Soc. 146 (2024) 6199–6208.
[15] X. Cheng, Y. Zuo, Y. Zhang, X. Zhao, L. Jia, J. Zhang, X. Li, Z. Wu, J. Wang, H. Lin, Superfast zincophilic ion conductor enables rapid interfacial desolvation kinetics for low-temperature zinc metal batteries, Adv. Sci 11 (2024) 2401629.
[16] J. Wang, H. Hu, L. Jia, J. Zhang, Q. Zhuang, L. Li, Y. Zhang, D. Wang, Q. Guan, H. Hu, M. Liu, L. Zhan, H. Adenusi, S. Passerini, H. Lin, Fast interfacial electrocatalytic desolvation enabling low-temperature and long-cycle-life aqueous Zn batteries, InfoMat 6 (2024) e12558.
[17] H. Du, R. Zhao, Y. Yang, Z. Liu, L. Qie, Y. Huang, High-capacity and long-life zinc electrodeposition enabled by a self-healable and desolvation shield for aqueous zinc-ion batteries, Angew. Chem. Int. Ed. 61 (2022) e202114789.
[18] Y. Zhang, Z. Cao, S. Liu, Z. Du, Y. Cui, J. Gu, Y. Shi, B. Li, S. Yang, Charge-enriched strategy based on MXene-based polypyrrole layers toward dendrite-free zinc metal anodes, Adv. Energy Mater. 12 (2022) 2103979.
[19] K. Fu, T. Liu, M. Xie, Y. Wu, Z. Li, Y. Xin, Y. Liao, C. Liu, H. Huang, D. Ma, F. Zeng, X. Liang, Water-lean inner helmholtz plane enabled by tetrahydropyran for highly reversible zinc metal anode, Adv. Funct.Mater 34 (2024) 2407895.
[20] Z. Wen, Z. Hu, X. Wang, Y. Zhang, W. Du, M. Ye, Y. Tang, X. Liu, C.C. Li, Weakening the space charge layer effect through tethered anion electrolyte and piezoelectric effect toward ultra-stable zinc anode, Adv. Mater. 36 (2024) 2407390.
[21] J. Cao, H. Wu, D. Zhang, D. Luo, L. Zhang, X. Yang, J. Qin, G. He, In-situ ultrafast construction of zinc tungstate interface layer for highly reversible zinc anodes, Angew. Chem. Int. Ed 63 (2024) e202319661.
[22] C. Li, X. Jiang, H. Qi, D. Chen, T. You, S. Huang, H. Yu, Y. Huang, M. Rao, G. Li, B. Xu, Y. Chen, L. Chen, Interfacial dual-modulation through deoxygenation effect and tuning hydrogen-bonding environment toward highly reversible Zn metal anodes, Energy Storage Mater 75 (2025) 104012.
[23] Y. Wang, Y. Chen, W. Liu, X. Ni, P. Qing, Q. Zhao, W. Wei, X. Ji, J. Ma, L. Chen, Uniform and dendrite-free zinc deposition enabled by in situ formed AgZn3 for the zinc metal anode, J. Mater. Chem. A 9 (2021) 8452–8461.
[24] L. Yao, J. Liu, F. Zhang, B. Wen, X. Chi, Y. Liu, Reconstruction of zinc-metal battery solvation structures operating from −50 ~ +100 °C, Nat. Commun. 15 (2024) 6249.
[25] Y. Zhou, G. Li, S. Feng, H. Qin, Q. Wang, F. Shen, P. Liu, Y. Huang, H. He, Regulating Zn ion desolvation and deposition chemistry toward durable and fast rechargeable Zn metal batteries, Adv. Sci. 10 (2022) 2205874.
[26] X. Huo, L. Xu, K. Xie, K. Zhang, J. Li, D. Wang, K. Shu, Cation-selective interface for kinetically enhanced dendrite-free Zn anodes, Adv. Energy Mater. 13 (2023) 2203066.
[27] W. Zhang, F. Guo, H. Mi, Z.S. Wu, C. Ji, C. Yang, J. Qiu, Kinetics-boosted effect enabled by zwitterionic hydrogel electrolyte for highly reversible zinc anode in zinc-ion hybrid micro-supercapacitors, Adv. Energy Mater. 12 (2022) 2202219.
[28] Z. Zhao, R. Wang, C. Peng, W. Chen, T. Wu, B. Hu, W. Weng, Y. Yao, J. Zeng, Z. Chen, P. Liu, Y. Liu, G. Li, J. Guo, H. Lu, Z. Guo, Horizontally arranged zinc platelet electrodeposits modulated by fluorinated covalent organic framework film for high-rate and durable aqueous zinc ion batteries, Nat. Commun. 12 (2021) 731.
[29] J. Ding, J. He, L. Chen, Y. Sun, Y. Xu, L.P. Lv, Y. Wang, Zincophilic sites enriched hydrogen-bonded organic framework as multifunctional regulating interfacial layers for stable zinc metal batteries, Angew. Chem. Int. Ed. 64 (2025) e202416271.
[30] Q. Zhang, P. Zhi, J. Zhang, S. Duan, X. Yao, S. Liu, Z. Sun, S.C. Jun, N. Zhao, L. Dai, L. Wang, X. Wu, Z. He, Q. Zhang, Engineering covalent organic frameworks toward advanced zinc-based batteries, Adv. Mater. 36 (2024) 2313152.
[31] Z. Jiang, Z. Du, R. Pan, F. Cui, G. Zhang, S. Lei, G. He, K. Yin, L. Sun, Electrosynthesis of metal-organic framework interlayer to realize highly stable and kinetics-enhanced Zn metal anode, Adv. Energy Mater. 14 (2024) 2402150.
[32] H. Yu, Y. Chen, W. Wei, X. Ji, L. Chen, Highly reversible zinc anode enabled by a cation-exchange coating with Zn-ion selective channels, ACS Nano 16 (2022) 6906–6915.
[33] D. Xu, Z. Wang, C. Liu, H. Li, F. Ouyang, B. Chen, W. Li, X. Ren, L. Bai, Z. Chang, A. Pan, H. Zhou, Water catchers within sub-nano channels promote step-by-step zinc-ion dehydration enable highly efficient aqueous zinc-metal batteries, Adv. Mater. 36 (2024) 2403765.
[34] C. Guo, J. Zhou, Y. Chen, H. Zhuang, Q. Li, J. Li, X. Tian, Y. Zhang, X. Yao, Y. Chen, S. Li, Y. Lan, Synergistic manipulation of hydrogen evolution and zinc ion flux in metal-covalent organic frameworks for dendrite-free Zn-based aqueous batteries, Angew. Chem. Int. Ed. 61 (2022) e202210871.
[35] Q. Chen, B. Gao, Z. Yang, Y. Li, Q. Zhai, Y. Jia, Q. Zhang, X. Gu, J. Zuo, L. Wang, T. Wang, P. Zhai, C. Yang, Y. Gong, Macroscopically uniform interface layer with Li^+ conductive channels for high-performance Li metal batteries, Nat. Commun. 15 (2024) 10045.

[36] Y. Shi, B. Li, Y. Zhang, Y. Cui, Z. Cao, Z. Du, J. Gu, K. Shen, S. Yang, Tortuosity modulation toward high-energy and high-power lithium metal batteries, Adv. Energy Mater 11 (2021) 2003663.
[37] H. Bian, G. Xue, D. Bin, S. Jia, Q. Zhou, H. Lu, X. Meng, Design of porous organic polymer ASEIs for Zn anode protection and ion migration regulation, Adv. Funct. Mater. (2024) 2417189.
[38] J. Su, X. Yin, H. Zhao, H. Yang, D. Yang, L. He, M. Wang, S. Jin, K. Zhao, Y. Wang, Y. Wei, Temperature-dependent nucleation and electrochemical performance of Zn metal anodes, Nano Lett. 22 (2022) 1549–1556.
[39] F. Li, L. Yu, Q. Hu, S. Guo, Y. Mei, Q. Liu, Y. He, X. Hu, Fabricating low-temperature-tolerant and durable Zn-ion capacitors via modulation of co-solvent molecular interaction and cation solvation, Sci. China Mater. 64 (2021) 1609–1620.
[40] S. You, Q. Deng, Z. Wang, Y. Chu, Y. Xu, J. Lu, C. Yang, Achieving highly stable Zn metal anodes at low temperature via regulating electrolyte solvation structure, Adv. Mater. 36 (2024) 2402245.
[41] K. Zhao, G. Fan, J. Liu, F. Liu, J. Li, X. Zhou, Y. Ni, M. Yu, Y.-M. Zhang, H. Su, Q. Liu, F. Cheng, Boosting the kinetics and stability of Zn anodes in aqueous electrolytes with supramolecular cyclodextrin additives, J. Am. Chem. Soc 144 (2022) 11129–11137.
[42] D. Wang, D. Lv, H. Peng, N. Wang, H. Liu, J. Yang, Y. Qian, Site-selective adsorption on ZnF_2/Ag coated Zn for advanced aqueous zinc–Metal batteries at low temperature, Nano Lett 22 (2022) 1750–1758.
[43] S. Chen, J. Chen, X. Liao, Y. Li, W. Wang, R. Huang, T. Zhao, S. Yan, Z. Yan, F. Cheng, H. Wang, Enabling low-temperature and high-rate Zn metal batteries by activating Zn nucleation with single-atomic sites, ACS Energy Lett. 7 (2022) 4028–4035.
[44] F. Bu, Y. Gao, W. Zhao, Q. Cao, Y. Deng, J. Chen, J. Pu, J. Yang, Y. Wang, N. Yang, T. Meng, X. Liu, C. Guan, Bio-inspired trace hydroxyl-rich electrolyte additives for high-rate and stable Zn-ion batteries at low temperatures, Angew. Chem. Int. Ed 63 (2024) e202318496.
[45] Y. Li, Y. Wang, Y. Xu, W. Tian, J. Wang, L. Cheng, H. Yue, R. Ji, Q. Zhu, H. Yuan, H. Wang, Dynamic Biomolecular, Mask" stabilizes Zn anode, Small 18 (2022) 2202214.
[46] Z. Zheng, S. Guo, M. Yan, Y. Luo, F. Cao, A functional Janus Ag nanowires/bacterial cellulose separator for high-performance dendrite-free zinc anode under harsh conditions, Adv. Mater. 35 (2023) 2304667.
[47] J. Wang, J. Zhang, J. Wu, M. Huang, L. Jia, L. Li, Y. Zhang, H. Hu, F. Liu, Q. Guan, M. Liu, H. Adenusi, H. Lin, S. Passerini, Interfacial "single-atom-in-defects" catalysts accelerating Li+ desolvation kinetics for long-lifespan lithium-metal batteries, Adv. Mater. 35 (2023) 2302828.
[48] J. Wang, J. Zhang, Y. Zhang, H. Li, P. Chen, C. You, M. Liu, H. Lin, S. Passerini, Atom-level tandem catalysis in lithium metal batteries, Adv. Mater. 36 (2024) 2402792.
[49] J. Wang, H. Liu, J. Zhang, Q. Xiao, C. Wang, Y. Zhang, M. Liu, Q. Kang, L. Jia, D. Wang, Q. Li, W. Duan, H. Adenusi, S. Passerini, Y. Zhang, H. Lin, Polysulfide-mediated solvation shell reorganization for fast Li+ transfer probed by in-situ sum frequency generation spectroscopy, Energy Storage Mater 67 (2024) 103289.
[50] H. Yang, J. Wang, P. Zhang, X. Cheng, Q. Guan, J. Dong, B. Chen, L. Jia, J. Zhang, Y. Zhang, Y. Liu, H. Lin, Dielectric-ion-conductive $ZnNb_2O_6$ layer enabling rapid desolvation and diffusion for dendrite-free Zn metal batteries, J. Energy Chem. 100 (2025) 693–701.
[51] T. Yan, B. Wu, S. Liu, M. Tao, J. Liang, M. Li, C. Xiang, Z. Cui, L. Du, Z. Liang, H. Song, Sieving-type electric double layer with hydrogen bond interlocking to stable zinc metal anode, Angew. Chem. Int. Ed 63 (2024) e202411470.